ISSN 1061-933X, Colloid Journal, 2024, Vol. 86, No. 1, pp. 40–51. © Pleiades Publishing, Ltd., 2024.

Modification of Synthetic Valleriite Surface with Gold Nanoparticles: The Roles of Specific Adsorption and Zeta Potential

A. A. Karacharov[a, *], M. N. Likhatski[a], R. V. Borisov[a, c], E. V. Tomashevich[a], S. A. Vorobyev[a], and S. M. Zharkov[b, c]

[a] *Institute of Chemistry and Chemical Technology, Siberian Branch, Russian Academy of Sciences, Federal Research Center "Krasnoyarsk Scientific Center, Siberian Branch, Russian Academy of Sciences," Akademgorodok, Krasnoyarsk, 660036 Russia*

[b] *Kirensky Institute of Physics, Siberian Branch, Russian Academy of Sciences, Federal Research Center "Krasnoyarsk Scientific Center, Siberian Branch, Russian Academy of Sciences," Akademgorodok, Krasnoyarsk, 660036 Russia*

[c] *Siberian Federal University, Krasnoyarsk, 660041 Russia*

**e-mail: antonkaracharov@ya.ru*

Received September 28, 2023; revised November 9, 2023; accepted November 11, 2023

Abstract—Layered two-dimensional materials, whose properties dramatically differ from their bulk precursors, are of great theoretical and applied importance. Recently, a layered 2D material, an analog of a natural mineral, valleriite, in which quasi-monoatomic Cu–Fe–S sheets alternate with brucite-like ones, has been prepared using a simple hydrothermal synthesis procedure. The features of the electronic structure of these materials make it possible to propose them as new materials for a wide field of applications such as (electro)photocatalysis, high-capacity batteries, etc. In this work, nanocomposite materials have been prepared via immobilization of gold nanoparticles (AuNPs) from citrate hydrosols on the surface of the synthesized valleriites having different compositions of hydroxide layers, which control the surface charge density. According to X-ray photoelectron spectroscopy (XPS), transmission electron microscopy (TEM), energy-dispersive X-ray microanalysis (EDX), and selected area electron diffraction (SAED) data, AuNPs are immobilized on valleriite nanoflakes, which have lateral sizes of 150–200 nm and thicknesses of several tens of nanometers, as isolated metal nanoparticles with an average diameter of 11 nm. A small amount of aggregates indicates a high affinity of AuNPs for the valleriite surface. The amounts of immobilized gold are the same on all studied valleriites (~0.2%). This finding may be related to the simultaneous sorption of free citrate ions from the AuNP hydrosols, with these ions, according to zeta potential measurements, charging the surfaces of all studied valleriite samples to nearly the same negative value of –40 mV. According to the XPS data, the AuNPs immobilization markedly decreases the magnesium and oxygen contents on the surfaces of the synthesized valleriites due to the partial degradation/dissolution of the brucite layer. In addition, the amount of Fe^{3+} ions bound to OH groups decreases with a simultaneous increase in the fraction of Fe^{3+}–O species. The TEM data have confirmed the preservation of the layered structure of valleriites after the immobilization of AuNPs.

Keywords: synthetic valleriites, gold nanoparticles, X-ray photoelectron spectroscopy, transmission electron microscopy, zeta potential

DOI: 10.1134/S1061933X23601075

1. INTRODUCTION

The great interest in two-dimensional materials is due to their developed surface and a wide spectrum of electronic, magnetic, optical, catalytic, and other properties [1–4]. In addition to graphene, the family of 2D materials is represented by transition metal chalcogenides, metal carbides and nitrides (so-called MXenes), layered double hydroxides (LDHs) of Mg, Al, Fe, etc., with the quasi-atomic layers in the latter being retained by van der Waals forces [5–18]. Recently, we have obtained a new promising type of mixed-layer materials, whose structures are similar to valleriite and tochilinite, and found their unusual optical and magnetic properties [20–22]. The effects of doping (modifying) both magnesium hydroxide (brucite) layer with lithium or aluminum and simultaneously the sulfide and brucite layers (Co, Cr, Ni) have been studied, and it has been shown that the band gap width and the density of the states near the valence band top can be regulated by varying the nature and concentration of a dopant/modifier [23, 24].

The generation of electron–hole pairs is of fundamental importance for a number of applications, primarily for photocatalysis [25–27]. There are many works, in which composites of semiconductor particles with metal nanoparticles were used to improve the

efficiency of photocatalysts [28–35]. A number of mechanisms have been described for the enhancement of the efficiency of composite-type photocatalysts, among which an increase in the lifetime of electron–hole pairs via the capture of charge carriers by metal particles is most often considered [31, 32, 36–38].

Due to the unique physical and chemical properties, gold nanoparticles (AuNPs) are used in various fields of catalysis, analytics (chemical sensors and test systems), biomedical applications (biomarkers and carriers of biologically active compounds), etc. [25, 39–45]. Beginning from the pioneering work by Haruta et al., who showed the high catalytic activity of AuNPs deposited onto the surface of TiO_2 in low-temperature reactions of CO oxidation, the interest in the preparation and study of such catalysts based on AuNPs is continuously growing [45, 46]. Today, the immobilization of AuNPs on oxide carriers is widely used to produce hybrid materials for heterogeneous catalysis, including (electro)photocatalysis, sensors for the analysis of various media, etc. [26, 46–50]. Methods available for the synthesis of hybrid gold-containing materials include the techniques of coprecipitation, amorphous alloying, deposition of AuNPs from colloidal solutions, coprecipitation of $Au(OH)_3$ with metal oxides and hydroxides, and chemical deposition [26, 46, 48–50]. It has recently been shown that the spontaneous precipitation of gold onto oxides of copper(II) and iron(III) (hematite) from aqueous solutions containing liquid intermediates of $HAuCl_4$ reduction with sodium sulfide at a molar ratio of 1 : 3 is significantly more efficient than the precipitation from an initial $HAuCl_4$ solution [51].

The nature of a carrier used for the preparation of composite materials containing AuNPs has a significant effect on their physicochemical properties and, therefore, largely determines their application fields [27]. Besides TiO_2 and other *d*-metal oxides, carbon-based materials (activated carbon, thermally expanded carbon, etc.) or materials with semiconductor properties, e.g., sulfides and other metal chalcogenides, are used as substrates for the immobilization of AuNPs [28–32, 52–54]. Moreover, the deposition of AuNPs onto semiconductor substrates causes a change in the positions of the valence and conduction bands, thereby making it possible to regulate the band gap width of a substrate material and its optical properties, in particular, the frequency of the localized surface plasmon resonance, thereby increasing its efficiency in (electro)photocatalysis, photodegradation of organic substances in the presence of oxygen, and many other plasmon-mediated chemical reactions [31], as well as the conversion of solar energy [34–38, 55–58]. Thus, materials, such as valleriite, the properties of which can be efficiently tuned and controlled by varying their composition, size, (nano)particle morphology, and other parameters, can become a new class of 2D materials having a wide spectrum of potential applications.

The goal of this work was to study the effect of aluminum and/or lithium additives on the surface properties (zeta potential and chemical composition) of synthetic valleriite samples and the immobilization of gold nanoparticles from colloidal solutions. The objectives of the work also included studying the influence of a number of factors on the value of the zeta potential of valleriite particles: the number of washing cycles of freshly synthesized materials, the conditions of drying and grinding with the formation of dry powders, etc.

2. EXPERIMENTAL

2.1. Reagents Used to Synthesize Valleriite and Gold Nanoparticles

The following commercial reagents were used for the synthesis of AuNPs: a 0.025 M chloroauric acid solution (OAO Krastsvetmet, Krasnoyarsk, Russia) stabilized with 1 M HCl, solutions of trisodium citrate (0.05 M) and sodium hydroxide (0.1 M). All solutions were prepared using reagents of at least analytical grade.

The hydrothermal synthesis of valleriite was carried out using the following commercial reagents: $FeSO_4 \cdot 7H_2O$, $CuSO_4 \cdot 5H_2O$, $MgSO_4 \cdot 7H_2O$, $Al_2(SO_4)_3 \cdot 18H_2O$, $LiCl_3 \cdot H_2O$, $Na_2S \cdot 9H_2O$, and an aqueous 25% NH_4OH solution. All reagents were of at least reagent grade.

Deionized water with a resistance of at least 18 MΩ m (Milli-Q, MilliPore) was used to prepare solutions and wash samples in all experiments.

2.2. Synthesis Procedures

2.2.1. Procedure for the autoclave synthesis of valleriite. The procedure for the autoclave synthesis of pure sulfide–hydroxide materials is described in detail in our study [23]. In this work, the procedure was somewhat simplified. Calculated weighed portions (Table 1) of iron and copper sulfates taken in a stoichiometric ratio of 1 : 1 were placed into a quartz beaker and dissolved in a minimum amount of deionized water. The solution was transferred into a fluoroplastic test tube, and a freshly prepared saturated solution of sodium sulfide was added. To prepare the saturated solution, $Na_2S \cdot 9H_2O$ (15 mmol, 3.6 g), was dissolved in a minimum amount of deionized water (5–8 mL). After the reagents were mixed, a black precipitate characteristic of sulfides of these metals was formed. In parallel, a precipitate of magnesium hydroxide or a mixture of magnesium, aluminum, and/or lithium hydroxides was obtained in a beaker by precipitating them with a 25% ammonium hydroxide solution, which was added until pH 10–11 was reached. Then it was transferred into the fluoroplastic test tube, the air phase in the test tube was replaced with argon. The fluoroplastic insert was placed into a stainless steel housing and sealed. The reaction mixture was heated in an autoclave to 160°C under continuous stirring.

Table 1. Molar ratios of precursors for sample synthesis

Valleriite samples	Amounts of precursors, mmol					
	Fe	Cu	Mg	Al	Li	Na_2S
VL_1	2.0	2.0	2.0	–	–	15
VL_2 (doped with Al)	2.0	2.0	2.0	0.5	–	15
VL_3 (doped with Li)	2.0	2.0	2.0	–	0.5	15
VL_4 (doped with Al and Li)	2.0	2.0	2.0	0.5	0.5	15

The mixture was thermostated for 50 h; then, the autoclave was cooled, a black precipitate was separated in a CR4000 ultracentrifuge (Centurion Scientific, United Kingdom) at 4000 rpm for 15 min. The precipitate was washed 5 times by redispersing in deionized water followed by centrifuging. The zeta potential was measured at each stage of purification.

The precipitates were dried at 30°C in air for 3 days and attrited in an agate mortar. Then, they were studied by physicochemical methods.

2.2.2. Preparation of a colloidal solution of gold nanoparticles. Gold nanoparticles were synthesized by the method of citrate reduction of Au(III) in a solution of chloroauric acid ($HAuCl_4$) with citrate ions at a neutral pH value (the so-called Turkevich method) [59–61]. A typical synthesis procedure involved heating a 0.3 mM $HAuCl_4$ solution (33 mL) in a water bath to 75°C followed by rapid addition of a 0.01 M NaOH solution (5 mL) of and a 0.01 M sodium citrate solution (0.610 mL). The resulting solution was heated in a water bath at 75°C (for nearly 30 min) until the solution acquired a ruby red color indicating the formation of final spherical gold nanoparticles with an average diameter of 21 ± 10 nm and a zeta potential value of –35 mV [59].

2.3. Immobilization of Gold Nanoparticles on Valleriite

To immobilize gold nanoparticles, a sample of dry valleriite powder (5 mg) was redispersed for 3 min in a small volume of water (about 1 mL) using a Sapphire UZV-1.3 ultrasonic bath (Sapphire, Russia) operating at a frequency of 35 kHz and a power of 50 W. An AuNP sol (30 mL) was added to the resulting suspension. The sorption was carried out under continuous stirring on a magnetic stirrer for 45 min. The precipitate was then separated from the mother solution by centrifugation at 4000 rpm for 8 min using a CR4000 ultracentrifuge (Centurion Scientific, United Kingdom). The resulting precipitate was washed 3 times by redispersing in deionized water followed by centrifugation at 5000 rpm.

2.4. Characterization of Samples

2.4.1. Measurement of zeta potentials. To determine the zeta potential value at each stage of purification of valleriite samples, a sample (0.5 mL) of a suspension was taken, dispersed in an aqueous 5 mM KCl solution (50 mL), which served as a background electrolyte, and the zeta potential of the particles was measured at 25°C with a Zetasizer Nano ZS particle size and zeta potential analyzer (Malvern Instruments, United Kingdom) operating at a scattering angle of 173° in a DTS 1070 polycarbonate cell equipped with Pd electrodes.

In the case of dried valleriite samples, to measure the zeta potential, a precipitate (0.5 mg) was preliminarily redispersed in a 1 mM KCl solution (50 mL) using a Sapphire UZV-1.3 ultrasonic bath (35 kHz, 50 W, 3 min). In addition, sodium citrate-containing samples were analyzed.

2.4.2. Procedure for determining the ratio of metals in valleriite. The ratio between the metals (Fe, Cu, Mg) in the samples was determined by atomic absorption analysis performed with an AAnalyst-400 spectrometer (Perkin Elmer, United States). For this purpose, a weighed portion of the material (10 ± 0.01 mg) was dissolved upon heating in 6 M hydrochloric acid (distilled isothermally), while adding hydrogen peroxide until complete dissolution. The solution was transferred into a graduated flask, the volume was brought to the mark with deionized water, and the sample analyzed. The contents of Al and Li in the solution were determined by inductively coupled plasma mass spectrometry (MS-ICP) with a 7500a instrument (Agilent, United States). The molar ratios between the metals were calculated relative to iron.

2.4.3. Transmission electron microscopy. Transmission electron microscopy (TEM) micrographs, energy-dispersive X-ray microanalysis (EDX) data, and selected area electron diffraction (SAED) patterns were obtained using a JEM 2100 transmission electron microscope (JEOL, Japan) operating at an accelerating voltage of 200 kV. Sample preparation for the study involved dispersing a small amount of a wet paste in distilled water under sonication for 30 min. A droplet of the resulting suspension was applied onto an EMCN Formvar ultrathin carbon film on a copper grid (Zhejiang, China) for 10 s; then, the droplet was removed with filter paper.

2.4.4. X-ray photoelectron spectroscopy. Photoelectron spectra were recorded using a SPECS spectrometer (SPECS GmbH, Germany) equipped with

a PHOIBOS 150 MCD9 hemispherical energy analyzer upon excitation by monochromatic radiation of an X-ray tube equipped with an aluminum anode (AlK_α-radiation, 1486.7 eV) operating at a power of 180 W and a tube voltage of 12.5 kV. The pressure in the analytical chamber was approximately 10^{-9} mbar. Survey spectra were recorded with a step of 0.5 eV at an energy analyzer transmission energy of 20 eV; the lines of individual elements (high-resolution spectra) were recorded with a step of 0.05 eV at a transmission energy of 8 eV. The C 1*s* line of a carbon contaminant layer with a binding energy (BE) of 284.7 eV was used as an internal reference to take into account electrostatic charging. Atomic concentrations of the elements were determined from the survey spectra with allowance for empirical sensitivity coefficients [62] taken from the database of the CasaXPS software package (version 2.3.16, Casa Software, Teignmouth, United Kingdom).

Element lines in the high-resolution spectra were deconvoluted with the help of the CasaXPS program using the Gauss–Lorentz line shape after Shirley background subtraction. The Fe 2*p* spectra were approximated by three sets of multiplet lines (four narrow lines and one wider line that corresponded to the shake-up satellite) for Fe^{3+} cations bonded to hydroxide, oxide, and sulfide anions; possible contributions from Fe^{2+} were also taken into account [63]. The S $2p_{3/2,1/2}$ and Au $4f_{7/2,5/2}$ bands were approximated after background subtraction according to Shirley by doublet lines using the Voight function with spin–orbit splittings of 1.19 and 3.67 eV and area ratios of 0.5 and 0.75, respectively. It is of importance to note that, due to the superposition of the Mg 2*s* line on the Au $4f_{5/2}$ doublet component of the 4*f* line of Au, the amount of gold was determined and the deconvolution into components was carried out focusing on the shape and intensity of the Au $4f_{7/2}$ second doublet component.

A sample to be examined by X-ray photoelectron spectroscopy (XPS) was applied in the form of a wet paste with a spatula as a uniform layer onto the surface of a titanium plate and dried in air. Then, the sample was transferred into the lock chamber of the spectrometer for complete drying.

3. RESULTS AND DISCUSSION

3. 1. Measurements of Zeta Potentials of Freshly Synthesized Samples

According to the results of measuring zeta potentials (Fig. 1), the successive washing of freshly synthesized valleriites significantly decreased their absolute values probably due to the removal of background ions from both the solution and the valleriite surface. In the course of washing, a significant decrease in the negative value of the zeta potential was observed. After the fifth washing cycle, a positive zeta potential value (+7.8 mV) was found only for the aluminum-doped valleriite sample. A decrease in the absolute value of the zeta potential indicates a decrease in the aggregative stability of the resulting suspensions and an increase in the rate of their separation, as is clearly seen in the presented photograph (see Fig. 1). Valleriite doping with aluminum leads to a shift in the zeta potential to the positive region, while the addition of lithium has almost no effect as compared with pure valleriite. The maximum positive zeta potential of aluminum-doped valleriite after fivefold washing is apparently reached due to the easiest desorption of anionic adsorbates (hydrosulfide and di- and polysulfide ions, as well as oxygen-containing anions) from the surface of the hydroxide layer. This becomes clear after the analysis of the published values of the isoelectric points of two-layer hydroxides [64], which shows that such a layer must have the lowest positive value of the surface charge density in the series of the studied valleriites and, hence, weaker retain the layer of counterions.

As can be seen from the data presented in Fig. 1, the drying of valleriite pastes, which yields dry samples, leads to a change in the values of their zeta potentials, measured under the same conditions. The zeta potential values become positive for all samples with the exception of lithium-doped valleriite (–1.7 mV). The changes observed in the zeta potential in the course of drying seem to be associated with the processes of particle aggregation and, possibly, with the oxidation of the surface sulfide layers of valleriite [19, 23, 24].

Apparently, the shift in the zeta potential to the positive region for valleriite samples, especially for dry powders, will facilitate the immobilization (sorption) of gold nanoparticles on their surfaces, because these nanoparticles have a negative zeta potential (on average, –35 mV). It should be taken into account that, along with metallic gold nanoparticles, Na^+, Cl^-, and, especially, citrate ions and citrate oxidation products are present in the colloidal solutions, because citrate is taken in a threefold excess relative to $HAuCl_4$.

3.2. Composition and Structure of Synthesized Materials

The ratio between the metals (Fe, Cu, and Mg) in the synthesized samples, as determined by atomic absorption analysis, is presented in Table 2.

Note that the overall composition does not enable us to determine the distribution of the metals between the layers; however, it evidently indicates that the ratio between iron, copper, and magnesium in the samples is in close correlation with the initial one. Aluminum and lithium are, most probably, included into the structure of the material only partially. The sulfur content in the samples was not determined.

Unlike atomic absorption analysis, XPS is a surface-sensitive method. Table 3 presents the data on the surface concentrations of the elements calculated from the survey XPS spectra measured for valleriite samples

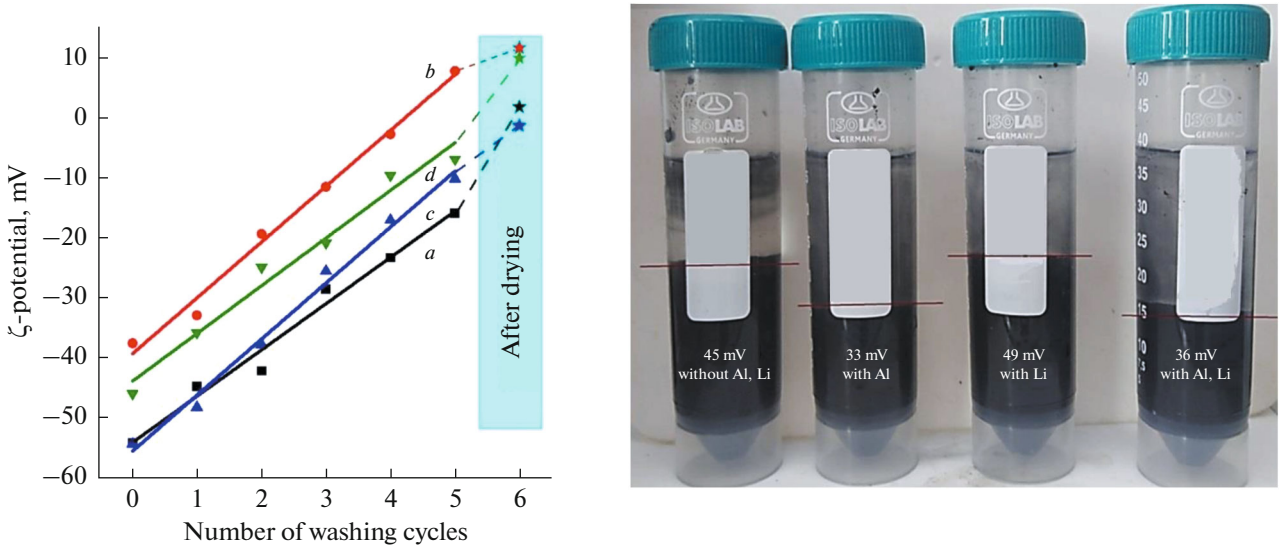

Fig. 1. Dependence of the zeta potential on the number of washing cycles (left) for freshly synthesized samples of (a) pure valleriite and that doped with (b) aluminum, (c) lithium and (d) a lithium–aluminum mixture. The values of the zeta potentials are presented for valleriite samples after drying and subsequent redispersion in a 0.05 M KCl solution. Photographs (right) of the synthesized materials after first cycle of washing with deionized water. Settling time is 5 min. Red lines indicate the boundaries of clarification. The given values of the zeta potentials were measured using the method described in the Experimental section.

before and after their contact with colloidal solutions of AuNPs.

The presented data suggest that AuNPs are immobilized on the surface of valleriite samples in small amounts. According to the intensities of the Au $4f_{7/2}$ lines, the highest gold surface concentration of 0.26 at % corresponds to the sample doped with an aluminum–lithium mixture, while the lowest concentration of 0.17 at % is observed for the sample of pure valleriite. For valleriite samples doped with either aluminum or lithium, the gold content is the same and amounts to 0.22 at %. Thus, there is no reliable correlation between the values of the zeta potential of valleriite samples and the amounts of gold immobilized on their surfaces in the form of metallic nanoparticles.

The following regularities can be identified for the changes in the concentrations of other elements on the surfaces of the samples during the sorption of AuNPs (Table 3). For all samples, the sorption of AuNPs causes a decrease in the contents of magnesium and oxygen on the surface probably due to the partial degradation of the brucite layer and an increase in the carbon content due to the sorption of free citrate ions and their oxidation products, as well as those immobilized on the surface of AuNPs. The iron content does not increase significantly. Note that, for pure valleriite and valleriite doped with aluminum, the surface concentrations of copper and sulfur slightly decrease. In turn, for valleriite doped with lithium or a lithium–aluminum mixture, the concentrations of copper and sulfur, on the contrary, increase apparently due to the partial dissolution of the brucite layer.

The Au 4*f* XPS spectrum (Fig. 2) is approximated by one doublet line with the binding energy of the Au $4f_{7/2}$ component equal to 84 eV, which corresponds to gold in the zero oxidation state. Thus, according to the XPS data, gold is immobilized on the surface of valleriite samples in the form of metal nanoparticles and does not contain other forms of gold in intermediate oxidation states (Figs. 2a, 2d, 2g, 2j).

The 2*p* line (Fig. 2) of iron was deconvoluted using three multiplet sets consisting of five lines, with the

Table 2. Molar ratios of metals in sulfide–hydroxide materials

Valleriite samples	Molar ratio of metals				
	Fe	Cu	Mg	Al	Li
VL_1	2.0	1.95	1.97	Absent	Absent
VL_2 (doped with Al)	2.0	1.98	1.95	0.15	Absent
VL_3 (doped with Li)	2.0	1.96	1.94	Absent	0.18
VL_4 (doped with Al and Li)	2.0	1.98	1.92	0.12	0.21

Table 3. Surface concentrations of elements in valleriite samples before (unfilled columns) and after (filled columns) sorption of AuNPs

Valleriite samples	Concentration, at %													
	Cu		Fe		O		C		S		Mg		Au	
VL_1	9.4	7.1	6.8	7.1	46	29.8	11.9	35.9	15.6	14.5	10.4	8.7	–	0.17
VL_2 (Al-doped)	6.4	9.6	4.4	6.3	44.1	37.8	14.2	20.4	15.3	16.9	15.6	8.7	–	0.22
VL_3 (Li-doped)	6.1	14.1	5.3	6.6	46.3	31.9	13.9	15.3	14	22.7	14.4	9.2	–	0.22
VL_4 (Al- and Li- doped)	7.3	11.3	5.1	5.2	45.7	36.7	11.5	13.4	15.9	23.3	14.5	9.8	–	0.26

maximum of the first line at 708, 710, and 711–712 eV for that bound to sulfide, oxide, and hydroxide anions, respectively.

Fitting of the Fe 2*p* spectra for the initial minerals have shown that in the samples iron is bound mainly to sulfide (Fe^{3+}–S) and hydroxide (Fe^{3+}–OH) anions. As we have shown previously [23], the incorporation of aluminum reduces the concentration of Fe^{3+}–OH bonds in the hydroxide layers, in contrast to doping with lithium, which does not change the content of the main forms of iron(III) in a sample (Figs. 2b, 2e). Comparing the results of measuring the zeta potentials of valleriite samples (see Section 3.1, Fig. 1) with the XPS data on the distribution of iron forms in the hydroxide layers, it can be concluded that the outer surfaces of the samples are represented by brucite-like layers, which impart positive zeta potentials to the surfaces of valleriite samples to this or that extent depending on the contribution of $Fe(3+)OH_6$ octahedrons. The contact with a colloidal solution of AuNPs reduces the content Fe^{3+} ions bound to hydroxide anions; this is especially noticeable for pure (undoped) and lithium-doped valleriite (Figs. 2b, 2c, 2e, 2f). The intensity of the components corresponding to Fe(3+) compounds bound to oxygen (Fe^{3+}–O) increases,

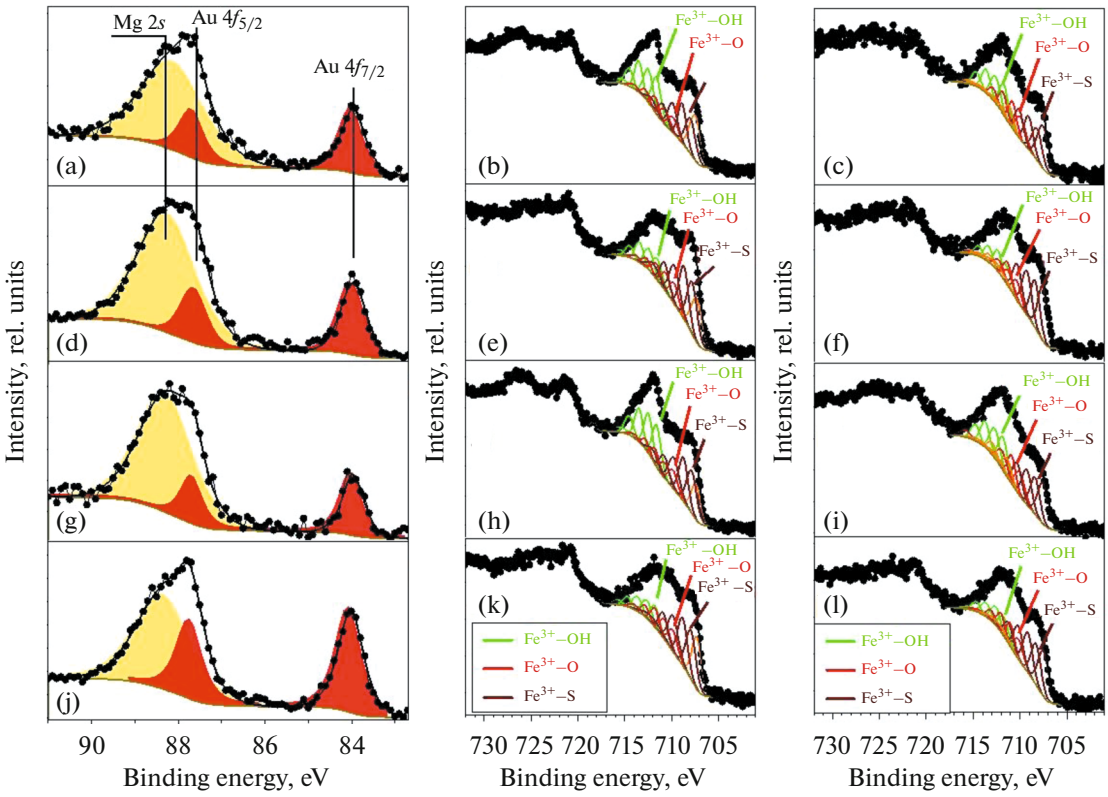

Fig. 2. Au $4f_{5/2,7/2}$ and Fe $2p_{3/2,1/2}$ XPS spectra for samples of (a, b, c) pure (undoped) valleriite and valleriite doped with (d, e, f) aluminum, (g, h, i) lithium, and (j, k, l) lithium–aluminum mixture (b, e, h, k) before and (a, c, d, f, g, i, j, l) after sorption of AuNPs from colloidal solutions.

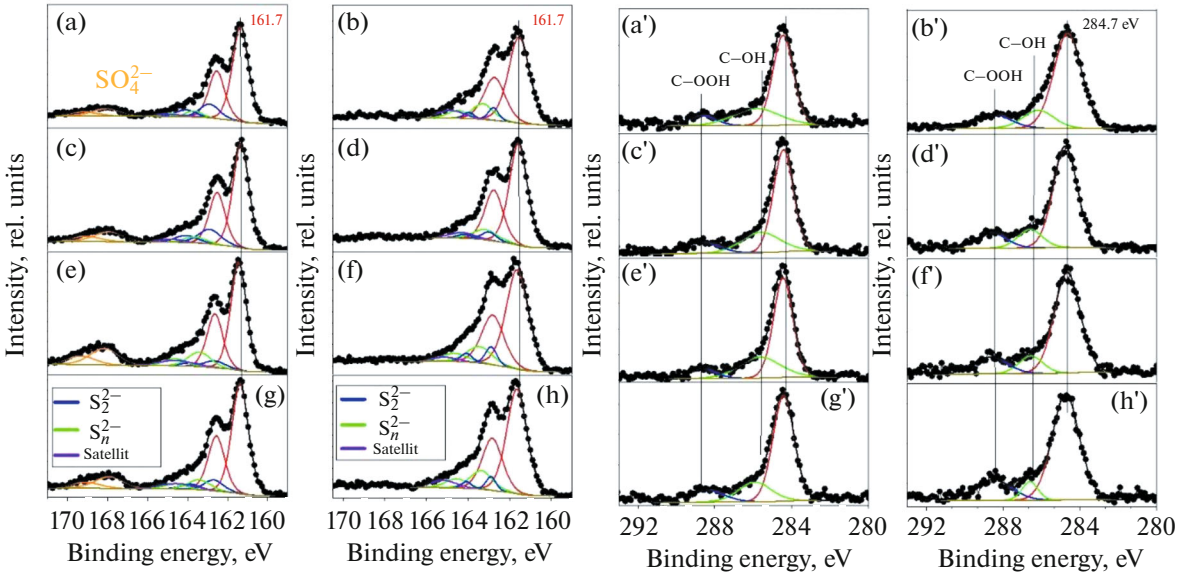

Fig. 3. S $2p_{3/2,1/2}$ and C 1*s* XPS spectra for samples of (a, b, a', b') pure (undoped) valleriite and that doped with (c, f, c', f ') aluminum, (g, h, g', h') lithium, and (i, j, i', j') lithium–aluminum mixture (a, a', c, c', e, e', g, g') before and (b, b', d, d', f, f ', h, h') after sorption of AuNPs from colloidal solutions.

while the content of iron sulfide remains almost unchanged (Figs. 2b, 2c, 2e, 2f, 2h, 2i, 2k, 2l).

According to the XPS data, sorption of AuNPs does not affect the shape of the Cu 2*p* line; while the main contribution (more than 80% of the total peak intensity) is made by the component with a BE of 932.5 ± 0.1 eV, which corresponds to copper that has the +1 oxidation state and is bound to sulfur. In addition, the absence of shake-up satellites at 944–948 eV in the 2*p* spectra of copper also confirms the absence of copper having the +2 oxidation state in the valleriite samples [65].

As in the case of the XPS spectra of copper, the oxygen 1*s* lines of the valleriite samples do not change significantly after sorption of AuNPs on them. The sorption of gold nanoparticles causes only a slight increase in the contribution of the component with a BE of 531.5 eV, which corresponds to oxygen contained in oxides (O^{2-} compounds).

The S 2*p* XPS spectra (Figs. 3a–3h) of the initial valleriite samples and those subjected to the contact with a colloidal solution of AuNPs contain the most intense doublet component (about 80% of the total line intensity) with a binding energy of the S $2p_{3/2}$ line equal to 161.7 ± 0.1 eV, which corresponds to sulfur in sulfide. In addition, the components of di- (BE 162.5 eV) and polysulfide (BE 163.5 eV) forms of sulfur are present in significantly smaller amounts. For a better fit, we used an additional broad line with a maximum at 164.5 eV attributed to the shake-up satellite, which results from the electron transfer to vacant Fe 3*d* orbitals [63, 65–67].

The S 2*p* spectra of the initial samples contain a doublet component with a BE of 169 eV corresponding to oxidized sulfur contained in sulfate ions. This component is absent in the sulfur spectra of valleriite samples that were brought in contact with colloidal solutions of AuNPs. Sulfate ions are most likely removed from the sample surfaces at the stage of washing off the pastes after the sorption of AuNPs is completed. The intensities of the lines corresponding to other forms of sulfur on the sample surfaces remain almost unchanged after the sorption of AuNPs.

The XPS spectra of the C 1*s* line (Figs. 3a'–3h') can be well fitted by three components: the most intense one with a BE of 284.7 eV, corresponding to the bonds of carbon in the composition of hydrocarbon contaminants, and less intense components with BEs of 286 and 288 eV, corresponding to the carbon atoms of C–OH and C–OOH groups, respectively.

It is important to note that, after the contact of valleriite samples with colloidal solutions of AuNPs, the content of C–OOH groups on the surface of the samples increases (Figs. 3b', 3d', 3f ', 3h'). That is, during the immobilization of AuNPs, citrate ions present in the colloidal solutions of AuNPs are markedly adsorbed in parallel. The adsorption of such a significant amount of citrate ions can lead to the sign reversal of the zeta potential of valleriite particles from positive to negative and an increase in its value in the negative region. Thus, the differences in the zeta potentials of the initial particles will be leveled out, and, consequently, the electrostatic attraction of negatively charged AuNPs to the surface of the minerals will decrease. In this regard, the surface zeta potentials of valleriite powders were measured after they were redispersed in

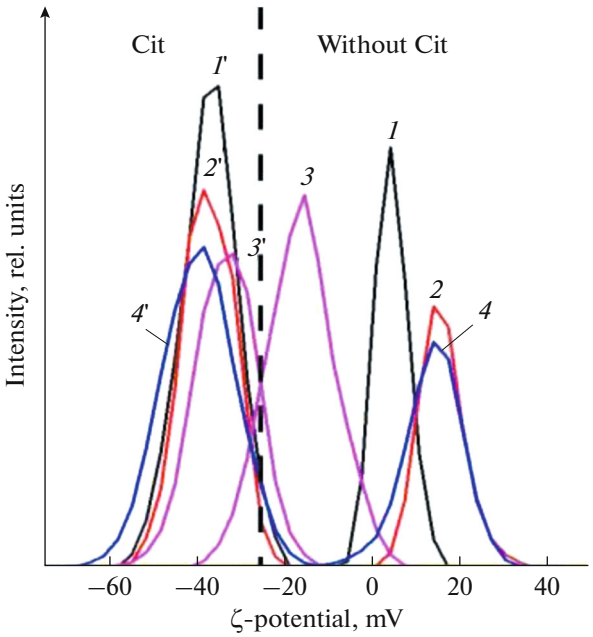

Fig. 4. Variations in the zeta potentials of dry powders (*1*–*4*) before and (*1'*–*4'*) after sorption of sodium citrate

an aqueous solution of KCl before and after the addition of citrate ions in a concentration of 3×10^{-4} M. The measurement results are presented in Fig. 4.

As can be seen in Fig. 4, the sorption of citrate ions radically changes the zeta potential of the surface of all valleriite samples shifting it to the negative region and making it almost the same and equal to –40 mV (Fig. 4, curves *1'*–*4'*). Thus, the initial difference in the zeta potential values of differently doped valleriite samples, which could affect the sorption of negatively charged AuNPs, is leveled by the sorption of free citrate ions, which are present even in the final colloidal solutions of AuNPs. Nevertheless, the sorption of citrate ions does not hinder the immobilization of AuNPs on the surface of valleriite samples in an amount sufficient to obtain nanocomposite materials.

In order to study the morphology and the character of the immobilization of gold nanoparticles on the surface of valleriite, a sample of aluminum-doped synthetic valleriite was studied by TEM with obtaining selected area electron diffraction (SAED) patterns and energy-dispersive X-ray (EDX) microanalysis (Fig. 5).

According to the obtained TEM data, gold nanoparticles are mainly immobilized on the surface of valleriite in the form of separately located spherical nanoparticles with an average diameter of 11 nm (Figs. 5a–5d). We believe that the adsorption of predominantly small gold nanoparticles on valleriite particles is due to the following factors: first, the smaller the particles the lower the potential barrier, because, according to the DLVO theory [68, 69], the force of mutual repulsion of colloidal particles is proportional to the particle radius. Second, particles with smaller radii have a higher frequency of collisions with other particles due to their higher mobility in a solution at a given temperature. Since the aggregation of lyophobic sols is thermodynamically favorable, their aggregative stability is determined only by the kinetic factor; hence, the aggregation rate directly depends on the frequency of collisions. Third, the fraction of coordinationally unsaturated atoms is larger for particles with smaller radii due to the large specific surface area.

Moreover, few aggregates are present on the sample surfaces, thereby indicating good adhesion of AuNPs to the valleriite surface, with this adhesion preventing them from aggregation during the sorption from colloidal solutions. The EDX data have confirmed that the detected particles consist of gold (Fig. 5f).

The interpretation of SAED patterns has shown the presence of rings characteristic of valleriite, as well as intense reflections (dots) corresponding to the crystal lattice of metallic gold (Fig. 5e).

CONCLUSIONS

It has been shown that successive washing of freshly synthesized valleriite samples leads to a decrease in the absolute value of their surface zeta potential. The drying procedure with obtaining dry powders of the minerals leads to the sign reversal of their surface zeta potential from negative to positive or a decrease to values close to zero upon subsequent redispersion in aqueous media, with the exception of the lithium-doped valleriite sample.

It has been found that the addition of aluminum as a dopant increases the positive charge of the valleriite surface by reducing the content of surface OH^- groups. In particular, the fraction of Fe^{3+} ions bonded to OH^- groups decreases due to their displacement into the sulfide layer. Doping with lithium has the opposite effect increasing the content of the surface OH-groups (the fraction of Fe^{3+}–OH bonds also increases) stabilizing the brucite layer of valleriite, thereby increasing the negative zeta potential of its surface.

XPS data have shown that AuNPs of colloidal solutions are immobilized on the surface of all synthetic valleriite samples in approximately equal amounts of about 0.2% irrespective of the sign and value of the zeta potential of the initial valleriite particle surface. This finding is explained by the previous sorption of free citrate ions and their oxidation products, which causes charging of the mineral surface to approximately the same value of –40 mV.

According to the TEM, EDX, SAED, and XPS data, AuNPs immobilized from colloidal solutions on the surface of valleriite are in the form of spherical metal nanoparticles with an average diameter of 11 nm arranged, predominantly, separately, thus indicating their high affinity for the surface of the synthetic minerals.

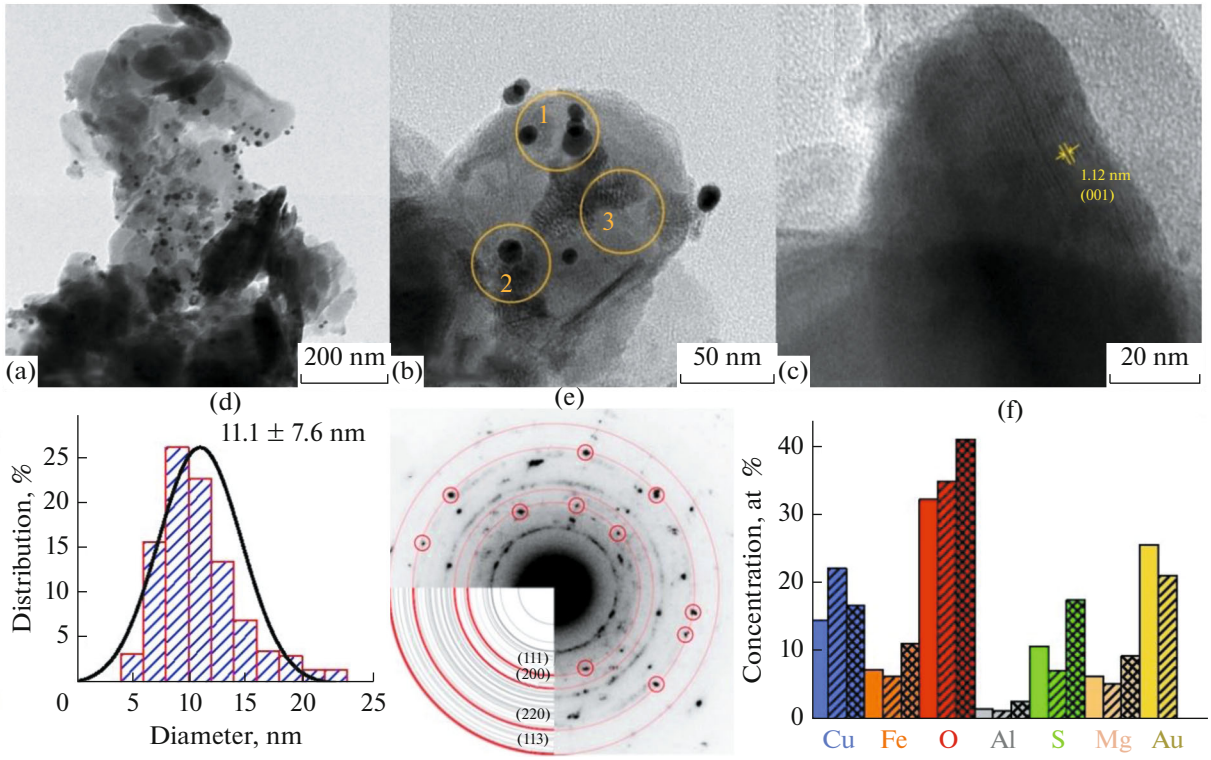

Fig. 5. (a–c) Typical TEM micrographs; (d) histogram of AuNP size distribution; (e) electron microdiffraction pattern for a sample of aluminum-doped valleriite after deposition of AuNPs from a colloidal solution; (f) data of energy-dispersive X-ray microanalysis for 3 regions indicated in panel (b): regions 1–3 correspond to unshaded, singly shaded, and doubly shaded columns, respectively.

ACKNOWLEDGMENTS

The equipment of the Krasnoyarsk Regional Center for Collective Use of the Krasnoyarsk Scientific Center, Siberian Branch, Russian Academy of Sciences, was used in the work. Electron microscopic studies were carried out at the Center of Collective Use of the Siberian Federal University.

FUNDING

This work was supported by the Russian Science Foundation project no. 22-13-00321.

CONFLICT OF INTEREST

The authors of this work declare that they have no conflicts of interest.

REFERENCES

1. Mikhlin, Yu.L., Likhatski, M.N., Borisov, R.V., et al., Metal chalcogenide–hydroxide hybrids as an emerging family of two-dimensional heterolayered materials: An early review, *Materials*, 2023, vol. 16, no. 19, p. 6381. https://doi.org/10.3390/ma16196381
2. Urade, A.R., Lahiri, I., and Suresh, K.S., Graphene properties, synthesis and applications: A review, *JOM*, 2023, vol. 75, no. 3, pp. 614–630. https://doi.org/10.1007/s11837-022-05505-8
3. Derakhshi, M., Daemi, S., Shahini, P., et al., Two-dimensional nanomaterials beyond graphene for biomedical applications, *J. Funct. Biomater.*, 2022, vol. 13, no. 1, p. 27. https://doi.org/10.3390/jfb13010027
4. Long, M., Wang, P., Fang, H., and Hu, W., Progress, challenges, and opportunities for 2D material based photodetectors, *Adv. Funct. Mater.*, 2019, vol. 29, no. 18, p. 1803807. https://doi.org/10.1002/adfm.201803807
5. Tiwari, S.K., Sahoo, S., Wang, N., and Huczko, A., Graphene research and their outputs: Status and prospect, *J. Sci.: Adv. Mater. Devices*, 2020, vol. 5, no. 1, pp. 10–29. https://doi.org/10.1016/j.jsamd.2020.01.006
6. Geim, A.K. and Grigorieva, I.V., Van der Waals heterostructures, *Nature*, 2013, vol. 499, no. 7459, pp. 419–425. https://doi.org/10.1038/nature12385
7. Xu, M., Lian, T., Shi, M., and Chen, H., Graphene-like two-dimensional materials, *Chem. Rev.*, 2013, vol. 113, no. 5, pp. 3766–3798. https://doi.org/10.1021/cr300263a
8. Zhang, K., Feng, Y., Wang, F., et al., Two-dimensional hexagonal boron nitride (2D-hBN): Synthesis, properties and applications, *J. Mater. Chem. C*, 2017, vol. 5,

no. 46, pp. 11992–12022.
https://doi.org/10.1039/C7TC04300G

9. Burch, K.S., Mandrus, D., and Park, J., Magnetism in two-dimensional van der Waals materials, *Nature*, 2018, vol. 563, no. 7729, pp. 47–52.
https://doi.org/10.1038/s41586-018-0631-z
10. Guo, Y., Zhou, S., and Zhao, J., Two-dimensional intrinsic ferromagnets with high Curie temperatures: Synthesis, physical properties and device applications, *J. Mater. Chem. C*, 2021, vol. 9, no. 19, pp. 6103–6121.
https://doi.org/10.1039/D1TC00415H
11. Cheng, Y.-W., Dai, J.-H., Zhang, Y.-M., and Song, Y., Two-dimensional, ordered, double transition metal carbides (MXenes): A new family of promising catalysts for the hydrogen evolution reaction, *J. Phys. Chem. C*, 2018, vol. 122, no. 49, pp. 28113–28122.
https://doi.org/10.1021/acs.jpcc.8b08914
12. Kim, H. and Alshareef, H.N., MXetronics: MXene-enabled electronic and photonic devices, *ACS Mater. Lett.*, 2020, vol. 2, no. 1, pp. 55–70.
https://doi.org/10.1021/acsmaterialslett.9b00419
13. Gao, M.-R., Xu, Y.-F., Jiang, J., and Yu, S.-H., Nanostructured metal chalcogenides: Synthesis, modification, and applications in energy conversion and storage devices, *Chem. Soc. Rev.*, 2013, vol. 42, no. 7, pp. 2986–3017.
https://doi.org/10.1039/C2CS35310E
14. Monga, D., Sharma, S., Shetti, N.P., et al., Advances in transition metal dichalcogenide-based two-dimensional nanomaterials, *Mater. Today Chem.*, 2021, vol. 19, p. 100399.
https://doi.org/10.1016/j.mtchem.2020.100399
15. Du, Z., Yang, S., Li, S., et al., Conversion of non-van der Waals solids to 2D transition-metal chalcogenides, *Nature*, 2020, vol. 577, no. 7791, pp. 492–496.
https://doi.org/10.1038/s41586-019-1904-x
16. Gao, T., Zhang, Q., Li, L., et al., 2D ternary chalcogenides, *Adv. Opt. Mater.*, 2018, vol. 6, no. 14, p. 1800058.
https://doi.org/10.1002/adom.201800058
17. He, Z. and Que, W., Molybdenum disulfide nanomaterials: Structures, properties, synthesis and recent progress on hydrogen evolution reaction, *Applied Materials Today*, 2016, vol. 3, pp. 23–56.
https://doi.org/10.1016/j.apmt.2016.02.001
18. Pekov, I. V., Yapaskurt, V. O., Polekhovsky, Y. S., et al., Ekplexite $(Nb,Mo)S_2{\cdot}(Mg_{1-x}Al_x)(OH)_{2+x}$, kaskasite $(Mo,Nb)S_2{\cdot}(Mg_{1-x}Al_x)(OH)_{2+x}$ and manganokaskasite $(Mo,Nb)S_2{\cdot}(Mn_{1-x}Al_x)(OH)_{2+x}$, three new valleriite-group mineral species from the Khibiny alkaline complex, Kola peninsula, Russia, *Mineral. Mag.*, 2014, vol. 78, no. 3, pp. 663–679.
https://doi.org/10.1180/minmag.2014.078.3.14
19. Mikhlin, Y.L., Romanchenko, A.S., Tomashevich, E.V., et al., XPS and XANES study of layered mineral valleriite, *J. Struct. Chem.*, 2017, vol. 58, no. 6, pp. 1137–1143.
https://doi.org/10.1134/S0022476617060105
20. Mikhlin, Y.L., Likhatski, M.N., Bayukov, O.A., et al., Valleriite, a natural two-dimensional composite: X-ray absorption, photoelectron and Mössbauer spectroscopy and magnetic characterization, *ACS Omega*, 2021, vol. 6, no. 11, pp. 7533–7543.
https://doi.org/10.1021/acsomega.0c06052
21. Mikhlin, Yu.L., Likhatski, M.N., Romanchenko, A.S., et al., Valleriite-containing ore from Kingash deposit (Siberia, Russia): Mössbauer and X-ray photoelectron spectroscopy characterization, thermal and interfacial properties, *J. Sib. Fed. Univ., Chem.*, 2022, vol. 15, no. 3, pp. 303–317.
https://doi.org/10.17516/1998-2836-0294
22. Karacharov, A. A., Borisov, R. V., Mikhlin, Y. L., et al., The study of bacterial leaching of synthetic valleriite-containing materials, *J. Sib. Fed. Univ., Chem.*, 2023, vol. 16, no. 2, pp. 300–311.
23. Mikhlin, Yu.L., Borisov, R.V., Vorobyev, S.A., et al., Synthesis and characterization of nanoscale composite particles formed by 2D layers of Cu–Fe sulfide and Mg-based hydroxide, *J. Mater. Chem. A*, 2022, vol. 10, no. 17, pp. 9621–9634.
https://doi.org/10.1039/D2TA00877G
24. Likhatski, M.N., Borisov, R.V., Fetisova, O.Yu., et al., Specificity of the thermal stability and reactivity of two-dimensional layered Cu–Fe sulfide-Mg-based hydroxide compounds (Valleriites), *ACS Omega*, 2023, vol. 8, no. 39, pp. 36109–36117.
https://doi.org/10.1021/acsomega.3c04274
25. Lee, M., Amaratunga, P., Kim, J., and Lee, D., TiO_2 nanoparticle photocatalysts modified with monolayer-protected gold clusters, *J. Phys. Chem. C*, 2010, vol. 114, no. 43, pp. 18366–18371.
https://doi.org/10.1021/jp106337k
26. Haruta, M., Gold as a novel catalyst in the 21st Century: Preparation, working mechanism and applications, *Gold Bull.*, 2004, vol. 37, nos. 1–2, pp. 27–36.
https://doi.org/10.1007/BF03215514
27. Campbell, C.T., Sharp, J.C., Yao, Y.X., et al., Insights into catalysis by gold nanoparticles and their support effects through surface science studies of model catalysts, *Faraday Discuss.*, 2011, vol. 152, pp. 227–239.
https://doi.org/10.1039/C1FD00033K
28. Linic, S., Chavez, S., and Elias, R., Flow and extraction of energy and charge carriers in hybrid plasmonic nanostructures, *Nat. Mater.*, 2021, vol. 20, no. 7, pp. 916–924.
https://doi.org/10.1038/s41563-020-00858-4
29. Sandroni, M., Wegner, K.D., Aldakov, D., and Reiss, P., Prospects of chalcopyrite-type nanocrystals for energy applications, *ACS Energy Lett.*, 2017, vol. 2, no. 5, pp. 1076–1088.
https://doi.org/10.1021/acsenergylett.7b00003
30. Spear, N.J., Hallman, K.A., Hernández-Pagán, E.A., et al., Enhanced broadband and harmonic upconversion from coupled semiconductor and metal nanoparticle films, *ACS Appl. Nano Mater.*, 2020, vol. 3, no. 4, pp. 3144–3150.
https://doi.org/10.1021/acsanm.0c00064
31. Torimoto, T., Horibe, H., Kameyama, T., et al., Plasmon-enhanced photocatalytic activity of cadmium sulfide nanoparticle immobilized on silica-coated gold particles, *J. Phys. Chem. Lett.*, 2011, vol. 2, no. 16, pp. 2057–2062.
https://doi.org/10.1021/jz2009049
32. Tagliabue, G., DuChene, J.S., Abdellah, M., et al., Ultrafast hot-hole injection modifies hot-electron dynamics in Au/*p*-GaN heterostructures, *Nat. Mater.*,

2020, vol. 19, pp. 1312–1318.
https://doi.org/10.1038/s41563-020-0737-1

33. Dorfs, D., Härtling, T., Miszta, K., et al., Reversible tunability of the near-infrared valence band plasmon resonance in Cu_2-XSe nanocrystals, *J. Am. Chem. Soc.*, 2011, vol. 133, no. 29, pp. 11175–11180. https://doi.org/10.1021/ja2016284
34. Guzman, F.V., Mercadal, P.A., Coronado, E.A., and Encina, E.R., Near-field enhancement contribution to the photoactivity in magnetite–gold hybrid nanostructures, *J. Phys. Chem. C*, 2019, vol. 123, no. 49, pp. 29891–29899. https://doi.org/10.1021/acs.jpcc.9b09421
35. Novotny, L. and van Hulst, N., Antennas for light, *Nat. Photonics*, 2011, vol. 5, no. 2, pp. 83–90. https://doi.org/10.1038/nphoton.2010.237
36. Zhan, C., Chen, X.J., Yi, J., et al., From plasmon-enhanced molecular spectroscopy to plasmon-mediated chemical reactions, *Nat. Rev. Chem.*, 2018, vol. 2, no. 9, pp. 216–230. https://doi.org/10.1038/s41570-018-0031-9
37. Hou, W. and Cronin, S.B., A review of surface plasmon resonance-enhanced photocatalysis, *Adv. Funct. Mater.*, 2012, vol. 23, no. 13, pp. 1612–1619. https://doi.org/10.1002/adfm.201202148
38. Agrawal, A., Cho, S.H., Zandi, O., et al., Localized surface plasmon resonance in semiconductor nanocrystals, *Chem. Rev.*, 2018, vol. 118, no. 6, pp. 3121–3207. https://doi.org/10.1021/acs.chemrev.7b00613
39. Sperling, R.A., Gil, P.R., Zhang, F., et al., Biological applications of gold nanoparticles, *Chem. Soc. Rev.*, 2008, vol. 37, no. 9, pp. 1896–1908. https://doi.org/10.1039/B712170A
40. Sardar, R., Funston, A.M., Mulvaney, P., and Murray, R.W., Gold nanoparticles: Past, present, and future, *Langmuir*, 2009, vol. 25, no. 24, pp. 13840–13851. https://doi.org/10.1021/la9019475
41. Falahatia M., Attar F., Sharifi M. et al. Gold nanomaterials as key suppliers in biological and chemical sensing, catalysis, and medicine, *BBA-General Subjects*. 2020, vol. 1864, no. 1, p. 129435. https://doi.org/10.1016/j.bbagen.2019.129435
42. Corma, A. and Garcia, H., Supported gold nanoparticles as catalysts for organic reactions, *Chem. Soc. Rev.*, 2008, vol. 37, no. 9, pp. 2096–2126. https://doi.org/10.1039/b707314n
43. Jain, P.K., Lee, K.S., El-Sayed, I.H., and El-Sayed, M.A., Calculated absorption and scattering properties of gold nanoparticles of different size, shape, and composition: Applications in biological imaging and biomedicine, *J. Phys. Chem. B*, 2006, vol. 110, no. 14, pp. 7238–7248. https://doi.org/10.1021/jp057170o
44. Wang, G., Zhang, C., He, X., et al., Detection of hydrazine based on nano-Au deposited on porous-TiO_2 film, *Electrochim. Acta*, 2010, vol. 55, no. 24, pp. 7204–7210. https://doi.org/10.1016/j.electacta.2010.07.053
45. Haruta, M., Kobayashi, T., Sano, H., and Yamada, N., Novel gold catalysts for the oxidation of carbon monoxide at a temperature far below 0°C, *Chem. Lett.*, 1987, vol. 16, no. 2, pp. 405–408. https://doi.org/10.1246/cl.1987.405
46. Haruta, M., Yamada, N., Kobayashi, T., and Ijima, S., Gold catalysts prepared by coprecipitation for low-temperature oxidation of hydrogen and of carbon monoxide, *J. Catal.*, 1989, vol. 115, no. 2, pp. 301–309. https://doi.org/10.1016/0021-9517(89)90034-1
47. Hutchings, G.J., Catalysis by gold, *Catal. Today*, 2005, vol. 100, nos. 1–2, pp. 55–61. https://doi.org/10.1016/j.cattod.2004.12.016
48. Primo, A., Corma, A., and Garcia, H., Titania supported gold nanoparticles as photocatalyst, *Phys. Chem. Chem. Phys.*, 2011, vol. 13, no. 3, pp. 886–910. https://doi.org/10.1039/c0cp00917b
49. Andreeva, D., Tabakova, T., Idakiev, V., et al., Au-Fe_2O_3 catalyst for water-gas shift reaction prepared by deposition–precipitation, *Appl. Catal., A*, 1998, vol. 169, no. 1, pp. 9–14. https://doi.org/10.1016/s0926-860x(97)00302-5
50. Haruta, M., Spiers memorial lecture: Role of perimeter interfaces in catalysis by gold nanoparticles, *Faraday Discuss.*, 2011, vol. 152, pp. 11–32. https://doi.org/10.1039/c1fd00107h
51. Likhatski, M.N., Karacharov, A.A., Romanchenko, A.S., et al., A comparative study of the deposition of nanoscale Au–S intermediate from aqueous solutions on CuO, TiO_2, and α-Fe_2O_3 surfaces, *J. Struct. Chem.*, 2021, vol. 62, no. 4, pp. 613–621. https://doi.org/10.1134/S0022476621040132
52. Borisov, R.V., Belousov, O.V., and Zhizhaev, A.M., Deposition of gold(III) from hydrochloric acid solutions on carbon nanotubes under hydrothermal conditions, *J. Sib. Fed. Univ., Chem.*, 2019, vol. 12, no. 4, pp. 494–502. https://doi.org/10.17516/1998-2836-0145
53. Borisov, R.V., Belousov, O.V., Likhatski, M.N., et al., Hydrothermal synthesis of Ir and Ir–Pd nanoparticles on carbon nanotubes, *Russ. Chem. Bull.*, 2022, vol. 71, no. 6, pp. 1164–1172. https://doi.org/10.1007/s11172-021-3242-z
54. Borisov, R.V., Belousov, O.V., Zhizhaev, A.M., et al., Synthesis of bimetallic nanoparticles Pd—Au and Pt–Au on carbon nanotubes in an autoclave, *Russ. Chem. Bull.*, 2021, vol. 70, no. 8, pp. 1474–1482. https://doi.org/10.1007/s11172-021-3242-z
55. Dement'eva, O.V. and Kartseva, M.E., Noble metal nanoparticles in biomedical thermoplasmonics, *Colloid J.*, 2023, vol. 85, no. 4, pp. 500–519. https://doi.org/10.1134/S1061933X23700187
56. Khan, S.A. and Misra, T.K., Investigation of newly developed 5-aminoisophthalate capped gold nanoparticles for degradation of azo-dyes, *Colloid J.*, 2023, vol. 85, no. 4, pp. 650–665. https://doi.org/10.1134/S1061933X22600622
57. Hussein, M., Structural and optomagnetic properties of Ni-doped ZnS synthesized by solvothermal method, *Colloid J.*, 2023, vol. 85, no. 4, pp. 666–672. https://doi.org/10.1134/S1061933X22600610
58. Aslam, U., Rao, V. G., Chavez, S., and Linic, S., Catalytic conversion of solar to chemical energy on plasmonic metal nanostructures, *Nat. Catal.*, 2018, vol. 1,

no. 9, pp. 656–665.
https://doi.org/10.1038/s41929-018-0138-x

59. Mikhlin, Yu.L., Karacharov, A.A., Likhatski, M.N., et al., Submicrometer intermediates in the citrate synthesis of gold nanoparticles: New insights into the nucleation and crystal growth mechanisms, *J. Colloid Interface Sci.*, 2011, vol. 362, no. 2, pp. 330–336.
https://doi.org/10.1016/j.jcis.2011.06.077

60. Turkevich, J., Stevenson, P.C., and Hillier, J., A study of the nucleation and growth processes in the synthesis of colloidal gold, *Discuss. Faraday Soc.*, 1951, vol. 11, pp. 55–75.
https://doi.org/10.1039/df9511100055

61. Frens, G., Controlled nucleation for the regulation of the particle size in monodispersed gold suspensions, *Nature: Physical Science*, 1973, vol. 241, no. 105, pp. 20–22.
https://doi.org/10.1038/physci241020a0

62. *Practical Surface Analysis by Auger and X-ray Photoelectron Spectroscopy*, Briggs, D.R. and Seah, M.P., Eds., Chichester: John Wiley and Sons Ltd, 1983.

63. Mikhlin, Y., Romanchenko, A., and Tomashevich, Y., Surface and interface analysis of iron sulfides in aqueous media using X-ray photoelectron spectroscopy of fast-frozen dispersions, *Appl. Surf. Sci.*, 2021, vol. 549, p. 149261.
https://doi.org/10.1016/j.apsusc.2021.149261

64. Nogueira, K.A.B., Cecilia, J.A., Santos, S.O., et al., Adsorption behavior of bovine serum albumin on Zn–Al and Mg–Al layered double hydroxides, *J. Sol-Gel Sci. Technol.*, 2016, vol. 80, no. 3, pp. 748–758.
https://doi.org/10.1007/s10971-016-4166-1

65. Nasluzov, V., Shor, A., Romanchenko, A., et al., DFT + U and low-temperature XPS studies of Fe-depleted chalcopyrite ($CuFeS_2$) surfaces: A focus on polysulfide species, *J. Phys. Chem. C*, 2019, vol. 123, no. 34, pp. 21031–21041.
https://doi.org/10.1021/acs.jpcc.9b06127

66. Mikhlin, Y., Nasluzov, V., Ivaneeva, A., et al., Formation, evolution and characteristics of copper sulfide nanoparticles in the reactions of aqueous cupric and sulfide ions, *Mater. Chem. Phys.*, 2020, vol. 255, p. 123600.
https://doi.org/10.1016/j.matchemphys.2020.123600

67. Mikhlin, Y., Nasluzov, V., Romanchenko, A., et al., Layered structure of the near-surface region of oxidized chalcopyrite ($CuFeS_2$): Hard X-ray photoelectron spectroscopy, X-ray absorption spectroscopy and DFT + U studies, *Phys. Chem. Chem. Phys.*, 2017, vol. 19, no. 4, pp. 2749–2759.
https://doi.org/10.1039/c6cp07598c

68. Verwey, E.J.W. and Overbeek, J.Th.G., *Theory of the Stability of Lyophobic Colloids*, New York-Amsterdam: Elsevier, 1948.

69. Deryagin, B.V., Churaev, N.V., and Muller, V.M., *Poverkhnostnye sily* (Surface Forces), Moscow: Nauka, 1987.